Synthesis and characterization of $Sr_{0.5}Zn_{0.5}Mn_2O_4$ powder for highly efficient visible light photocatalysis

Khawla Benyahia[1], Mohamed Badaoui[1], Hafida Sehil[2], Abdelkader Chougui[3], Abdel-Hamid I. Mourad[4,5,*], Soumaya Grira[6], Abdelkader Dehbi[7]

[1]*Synthesis and Catalysis Laboratory, University of Tiaret, BP P 78 Zaaroura, Tiaret, Algeria*

[2]*Department of Chemistry, Faculty of Sciences of the Matter, University of Tiaret, BP P78, Zaaroura, Tiaret, Algeria*

[3]*Department of Sciences and Technologies, Faculty of Applied Science, University of Tiaret, Algeria*

[4]*Mechanical and Aerospace Engineering Department, United Arab Emirates University, Al-Ain, P.O. Box 15551, UAE*

[5]*National Water and Energy Center, United Arab Emirates University, Al-Ain, P.O. Box 15551, UAE*

[6]*Chemical and Petroleum Engineering Department, United Arab Emirates University, Al-Ain, P.O. Box 15551, UAE*

[7]*Engineering Physics Laboratory, University of Tiaret, 14000, Tiaret, Algeria*

Received 15 April 2025; received in revised form 6 June 2025; accepted 20 June 2025

Abstract

Spinel oxide $Sr_{0.5}Zn_{0.5}Mn_2O_4$ powder was successfully synthesized using the ultrasonic process. A comprehensive characterization was conducted employing various analytical techniques, including X-ray diffraction (XRD), infrared spectroscopy (IR), UV-Vis spectroscopy, scanning electron microscopy (SEM), thermogravimetric analysis, energy-dispersive X-ray spectroscopy and point of zero charge measurements. The results of IR analysis confirmed the presence of Zn–O, Sr–O and Mn–O bonds, which are crucial for the structural integrity of the material. The XRD patterns showed enhanced crystallinity, while the band gap energy was determined to be 2.5 eV, as corroborated by UV-Vis spectroscopy. Additionally, the SEM analysis revealed that the particles exhibited uniformity in both size and shape, which is essential for consistent photocatalytic performance. Furthermore, the $Sr_{0.5}Zn_{0.5}Mn_2O_4$ was evaluated for its photocatalytic activity, specifically targeting the degradation of Congo red dye under visible light irradiation. The findings of the photocatalytic study demonstrated a significant improvement in degradation efficiency (99.37%), highlighting the potential application of $Sr_{0.5}Zn_{0.5}Mn_2O_4$ in environmental remediation. A detailed study on the influence of various parameters, including pH, the amount of catalyst and the initial concentration of dye was also conducted to optimize the photocatalytic process.

Keywords: *$Sr_{0.5}Zn_{0.5}Mn_2O_4$ powder, ultrasonic method, structure, photocatalysis, degradation, Congo red*

I. Introduction

Dyes play a pivotal role in various industries, contributing to the vibrancy and appeal of products we use daily. From textiles and leather to paints and plastics, these colourants are essential for enhancing the aesthetic value of goods. However, the widespread use of dyes comes with significant environmental concerns [1–13]. With over 10,000 different dye species in existence and an annual production surpassing 80 million tons, the potential for ecological harm is substantial. The primary concern lies in the fact that many dyes are classified as pollutants, particularly when they enter water bodies through industrial wastewater. These contaminants can lead to severe water quality issues, affecting aquatic ecosystems and human health [1,4–9].

Among the various dyes used in the textile industry, Congo red (RC) stands out as particularly

[*]Corresponding author: tel: +91 9934837317
e-mail: *ahmourad@uaeu.ac.ae*

toxic. Its stability and resistance to biodegradation make it a popular choice for colouring textiles. However, the extensive use of these dyes, along with textile industry effluent (TIE), poses significant health risks. When inhaled or ingested, RC has been linked to a range of serious health issues, including eye infections, respiratory tract ulcers, skin irritation, gastrointestinal problems and even cancer in both humans and animals [14–17].

To address these challenges, innovative solutions for wastewater treatment are needed. One promising approach involves the use of spinel oxides in photocatalytic processes [18–22]. Spinel oxides are semiconductors known for their unique structural properties, such as high thermal stability [23], excellent electronic conductivity [24–31] and the ability to absorb a wide range of light wavelengths. These properties make them highly effective photocatalyst for degrading organic pollutants, including hazardous dyes [32–39]. Their applications extend beyond wastewater treatment, encompassing fields such as solar energy conversion [40–43], gas sensing [44-46] and environmental remediation [47–55].

Spinel oxides have gained significant attention as highly effective photocatalysts for degrading organic pollutants, particularly hazardous dyes and other contaminants. Their unique structural and electronic properties enable efficient charge separation and strong visible light absorption, making them suitable for various environmental applications. Among these materials, $ZnMn_2O_4$ has emerged as a promising candidate due to its multifunctionality in wastewater treatment, renewable energy conversion and environmental remediation.

Several studies have investigated $ZnMn_2O_4$ for wastewater treatment, focusing on its ability to degrade organic pollutants. Fallatah *et al.* [56] synthesized $ZnMn_2O_4$ nanorods using a metal-organic framework (MOF)-derived method and reported impressive photocatalytic efficiency, achieving 94.25% degradation of rhodamine B and 90.52% of crystal violet. Sobhani *et al.* [57] synthesized $ZnMn_2O_4$ nanostructures via hydrothermal and co-precipitation methods, demonstrating a 92.43% decolorization rate of methyl violet (MV) under optimal conditions. Gherbi *et al.* [58] prepared Mg-doped $ZnMn_2O_4$ using a sol-gel method and found that increasing Mg content improved photocatalytic efficiency, achieving a 72% degradation rate for methylene blue (MB) under visible light irradiation. Mohammed Nazeer *et al.* [59] investigated $ZnFe_2O_4$/ZnO nanocomposites, achieving over 90% degradation of Congo red (RC) dye in 40 min under optimized conditions and Parastar Gharehlar *et al.* [60] synthesized MFe_2O_4/GO nanocomposites, where $CoFe_2O_4$/GO exhibited a remarkable 95.57% dye removal efficiency. Zala *et al.* [61] developed magnetically separable $CuFe_2O_4$ nanoparticles with enhanced photocatalytic activity under AM 1.5 G sunlight, optimizing their tetragonal phase to maximize organic dye degradation, including a 55% removal rate for methylene blue. While these studies demonstrate the high potential of spinel oxides in wastewater treatment, most research is limited to controlled laboratory conditions. Factors such as water composition, catalyst stability and regeneration efficiency remain largely unaddressed, highlighting the need for further investigations on real-world applications and scalability.

Beyond wastewater treatment, $ZnMn_2O_4$ and related spinel oxides have demonstrated potential in renewable energy conversion, gas sensing and environmental remediation. Yaqoubi *et al.* [62] developed a $CuMn_2O_4$/g-C_3N_4 heterojunction, which exhibited superior photocatalytic activity due to the enhanced charge carrier mobility and extended light absorption range. Shinde *et al.* [63] explored $ZnMn_2O_4$/MoS_2 heterostructures, demonstrating enhanced charge separation and improved photoelectrochemical performance, making them effective for both water splitting and pollutant removal. Liu *et al.* [64] fabricated ternary $ZnMn_2O_4$/$ZnIn_2S_4$ nanocomposites for photocatalytic hydrogen generation, showing their effectiveness in solar-driven water splitting. Morán-Lázaro *et al.* [65] investigated $ZnMn_2O_4$ for photovoltaic applications, further demonstrating its adaptability in energy-related fields. Deepika *et al.* [66] explored the use of $ZnMn_2O_4$ in next-generation photodetectors, leveraging its superior optoelectronic properties for improved light detection. Azmoodeh *et al.* [67] synthesized $ZnMn_2O_4$ for photocatalytic applications, achieving a 60% degradation rate for Cr(VI), indicating its potential for toxic metal remediation. Despite these promising developments, the practical integration of $ZnMn_2O_4$ into commercial energy systems and sensors remains a challenge. Issues such as material stability under prolonged operation, cost-effective synthesis methods and performance consistency under variable environmental conditions need to be addressed through further research and material optimization.

While $ZnMn_2O_4$ has demonstrated strong photocatalytic potential, other spinel oxides, such as $NiCo_2O_4$ and $ZnFe_2O_4$, also offer competitive advantages. $NiCo_2O_4$ exhibits robust stability and efficiency in chromium reduction, while $ZnFe_2O_4$/ZnO composites excel in rapid dye degradation. The choice of photocatalyst depends on factors such as pollutant type, reaction conditions and material cost. Despite their promising applications, $ZnMn_2O_4$-based photocatalysts face challenges related to stability, recyclability and large-scale production. One key limitation is the potential agglomeration of nanoparticles, which can reduce their photocatalytic activity over multiple cycles. Additionally, while laboratory-scale studies report high degradation efficiencies, real-world implementation requires further optimization in terms of catalyst durability, reusability and environmental impact assessments. Future research should focus on enhancing the long-term stability of $ZnMn_2O_4$ through surface modifications, heterostructuring and doping strategies. Additionally, exploring sustainable and cost-effective synthesis routes can facilitate large-scale deployment of these materials for environmental and energy applications. Overall, the multifunctional nature of $ZnMn_2O_4$ makes it a highly promising material for a diverse range of applications, from wastewater treatment and solar energy conversion to gas sensing and environmental remediation.

Based on the above literature, the work relevant to novel spinel oxide photocatalyst is lacking. Therefore, the main objective of this paper is to develop a novel $Sr_{0.5}Zn_{0.5}Mn_2O_4$ as a highly efficient photocatalyst. The synthesized $Sr_{0.5}Zn_{0.5}Mn_2O_4$ was extensively characterized using a range of physicochemical techniques, including Fourier-transform infrared spectroscopy, X-ray diffraction analysis, DTA/TGA analysis, elemental dispersive energy and scanning electron microscopy. Furthermore, the effects of varying concentration, pH, and weight on the photocatalytic study conditions and removal efficiencies were examined.

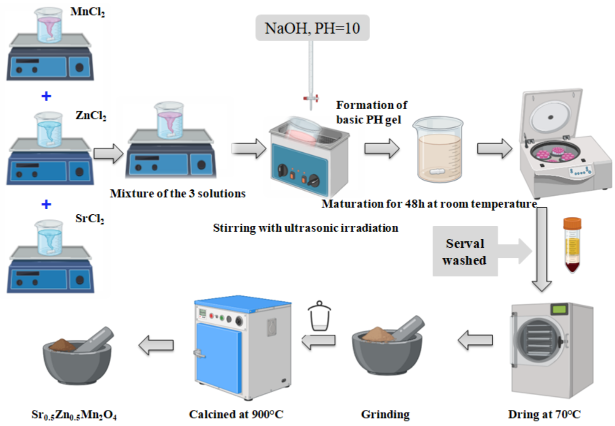

Figure 1. Schematic presentation of the synthesis procedure of $Sr_{0.5}Zn_{0.5}Mn_2O_4$ nanoparticles

II. Experimental

2.1. Sample preparation

Zinc chloride $ZnCl_2$, strontium chloride $SrCl_2$, manganese(II)-chloride 2-hydrate $MnCl_2 \times 2H_2O$ (Pro analysis, MERCK) and sodium hydroxide (Sigma-Aldrich) were used for the sample preparation. The $Sr_{0.5}Zn_{0.5}Mn_2O_4$ nanoparticles were synthesized via the sonochemical method. Precursor solution was obtained by dissolving of 1.58 g of $SrCl_2$, 0.81 g of $ZnCl_2$ and 3.79 g of $MnCl_2 \times 2H_2O$ in 240 ml of distilled water. Under constant stirring, 0.8 M of NaOH was added to this precursor solution and the resulting mixture was then subjected to high-intensity ultrasonic irradiation for 5 h at 60 °C. The $Sr_{0.5}Zn_{0.5}Mn_2O_4$ nanoparticles were separated by centrifugation, washed several times with distilled water to remove any residual sodium chloride (NaCl) and then dried at 70 °C for 48 h before a final calcination at 900 °C for 4 h. Schematic presentation of the synthesis procedure is shown in Fig. 1. The structure of the devloped oxide is demonstrated in Fig. 2.

2.2. Characterization methods

In order to identify functional groups, the produced samples were characterized using Fourier transform infrared spectroscopy (FTIR), which offers comprehensive insights into the molecular structure and chemical bonding, therefore facilitating the characterization and identification of chemical species. An FTIR spectrophotometer operated with Shimadzu IR spirit was used, with the wavelength adjusted from 400 cm^{-1} to 4000 cm^{-1}.

The crystallinity of the $Sr_{0.5}Zn_{0.5}Mn_2O_4$ powder was investigated using X-ray diffraction (XRD), which is required to obtain valuable information on the structural characteristics and level of crystalline organization. XRD patterns were obtained by Philips PW1830 diffractometer within the range of 2°–60°. The X-rays were generated using CuKα radiation (λ = 1.5406 Å) and a copper anticathode with current of 30 mA and voltage of 40 kV.

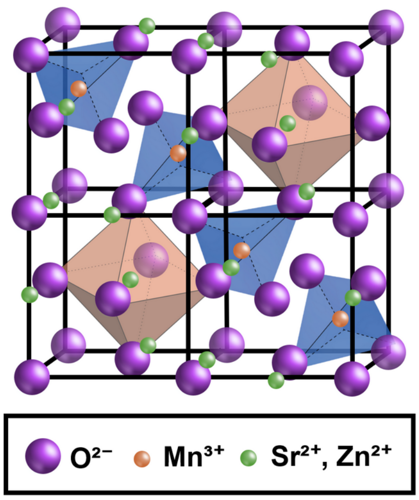

Figure 2. Structure of the developed $Sr_{0.5}Zn_{0.5}Mn_2O_4$

Differential thermal analysis (DTA) and thermogravimetric analysis (TGA) were performed using a Mettler Toledo instrument to further characterize the synthesized material. DTA provides information about phase transitions and thermal events occurring in the sample as a function of temperature, while TGA measures the weight loss of the material during heating.

Furthermore, the morphology of the $Sr_{0.5}Zn_{0.5}Mn_2O_4$ sample was analysed using a JEOL JSM 6000 scanning electron microscope (SEM). This technique yields high-resolution images that facilitate the analysis of surface characteristics and particle dimensions of the material.

Red Congo (RC) dye content in the supernatant solution was quantified using the UV-Vis-2401PC Shimadzu spectrophotometer both before and after the degradation procedure. The measurement was conducted at a wavelength of 497 nm. This methodology enables the quantification of the adsorption capacity and removal effectiveness of the catalyst material in the context of red Congo dye.

III. Results and discussion

3.1. Structural characterization

FTIR analysis

FTIR spectrum of the calcined $Sr_{0.5}Zn_{0.5}Mn_2O_4$ powder is presented in Fig. 3. The observed peaks at 504 cm^{-1} refer to the stretching vibration of the Mn–O bond in the MO_6 tetrahedra and the Zn–O bond in the MO_4 octahedra [68,69]. On the other hand, the band corresponding to the stretching of Sr–O is at 624 cm^{-1} [70]. Additionally, the low intensity band at 2375 cm^{-1} is assigned to the C–O bond of CO_2 which is present in the atmosphere. The FTIR results confirm the formation of $Sr_{0.5}Zn_{0.5}Mn_2O_4$ spinel structure.

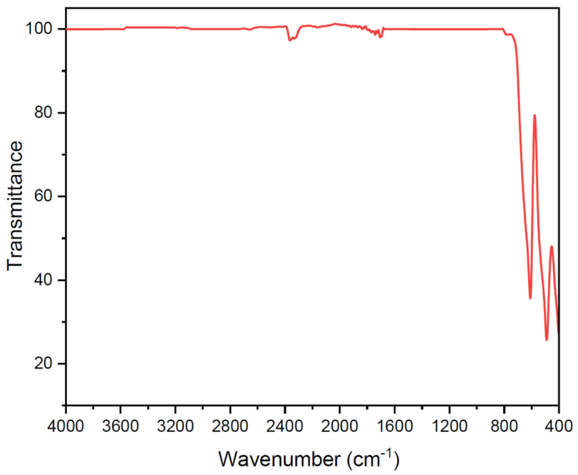

Figure 3. FTIR spectrum of $Sr_{0.5}Zn_{0.5}Mn_2O_4$ powder

XRD analysis

X-ray powder diffraction was used in order to investigate the crystal structure of the synthesized $Sr_{0.5}Zn_{0.5}Mn_2O_4$ powder calcined at 900 °C (Fig. 4). The significant peaks observed in XRD diffractogram are at 2θ values of 29.4°, 31°, 33, 36.34°, 45°, 54°, 58°, 62.5° and 74°, confirming the cubic spinel structure [71]. The $Sr_{0.5}Zn_{0.5}Mn_2O_4$ spinel structure forms a face-centred cubic (FCC) close-packed arrangement, where Sr^{2+}, Zn^{2+} and Mn^{3+} cations occupy: the octahedral sites (coordination 6, associated with Mn_2O_3) and 50% of the tetrahedral sites (coordination 4, derived from a mix of SrO and ZnO). Thus, the observed peaks for SrO, ZnO and Mn_2O_3 are consistent with the expected cations distribution in this spinel phase.

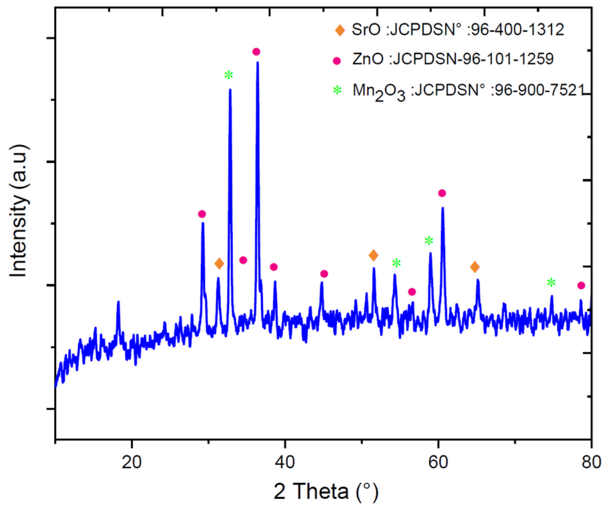

Figure 4. XRD pattern of $Sr_{0.5}Zn_{0.5}Mn_2O_4$ powder

The average crystallite size of the prepared materials was calculated using the Scherrer's formula:

$$D = \frac{0.9 \cdot \lambda}{\beta \cdot \cos\theta} \quad (1)$$

where D is the grain size, λ is the wavelength of the X-ray beam, θ is the diffraction angle and finally β is the full width at half of the maximum (FWHM). It is found that the average crystallite size of the calcined $Sr_{0.5}Zn_{0.5}Mn_2O_4$ powder is equal to 25.2 nm.

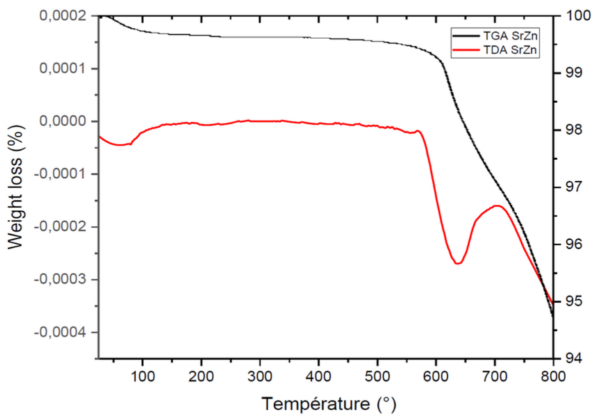

Figure 5. TGA thermograms of $Sr_{0.5}Zn_{0.5}Mn_2O_4$ powder

TGA analysis

Thermogravimetric analysis of the synthesized $Sr_{0.5}Zn_{0.5}Mn_2O_4$ presented in Fig. 5 provides information on the weight loss at different temperature ranges. Notably, a minor weight loss of 0.5% occurs between 50–100 °C, probably corresponding to evaporation of adsorbed water. In the temperature range of 570–704 °C a more significant weight loss of 3.3% can be attributed to the release of CO_2 which was confirmed with FTIR analysis and the decomposition of carbonate present within the material. Furthermore, a weight loss of 5.1% is observed between 704–800 °C, indicating additional thermal decomposition processes and formation of spinel strontium-zinc manganese [72].

UV-Vis spectroscopy

The absorbance spectrum of the $Sr_{0.5}Zn_{0.5}Mn_2O_4$ powder calcined at 900 °C, illustrated in Fig. 6, reveals absorbance within the visible spectrum. The energy band gap (E_g) is typically determined using the Kubelka-Munk equation [73] as follows:

$$\alpha h\nu = K\left(h\nu - E_g^{\ n}\right) \tag{2}$$

where K represents the proportionality constant, h is Planck's constant, ν signifies the frequency of the photons and n indicates the type of electronic transition. The intercept on the energy axis from the linear segment of the graph provides the average value of the band gap.

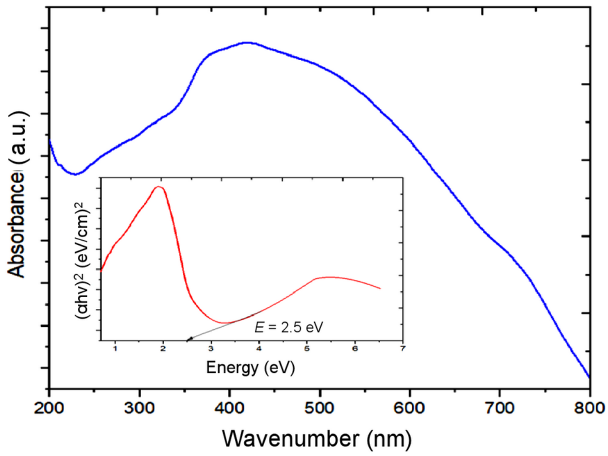

Figure 6. Optical band gap of $Sr_{0.5}Zn_{0.5}Mn_2O_4$

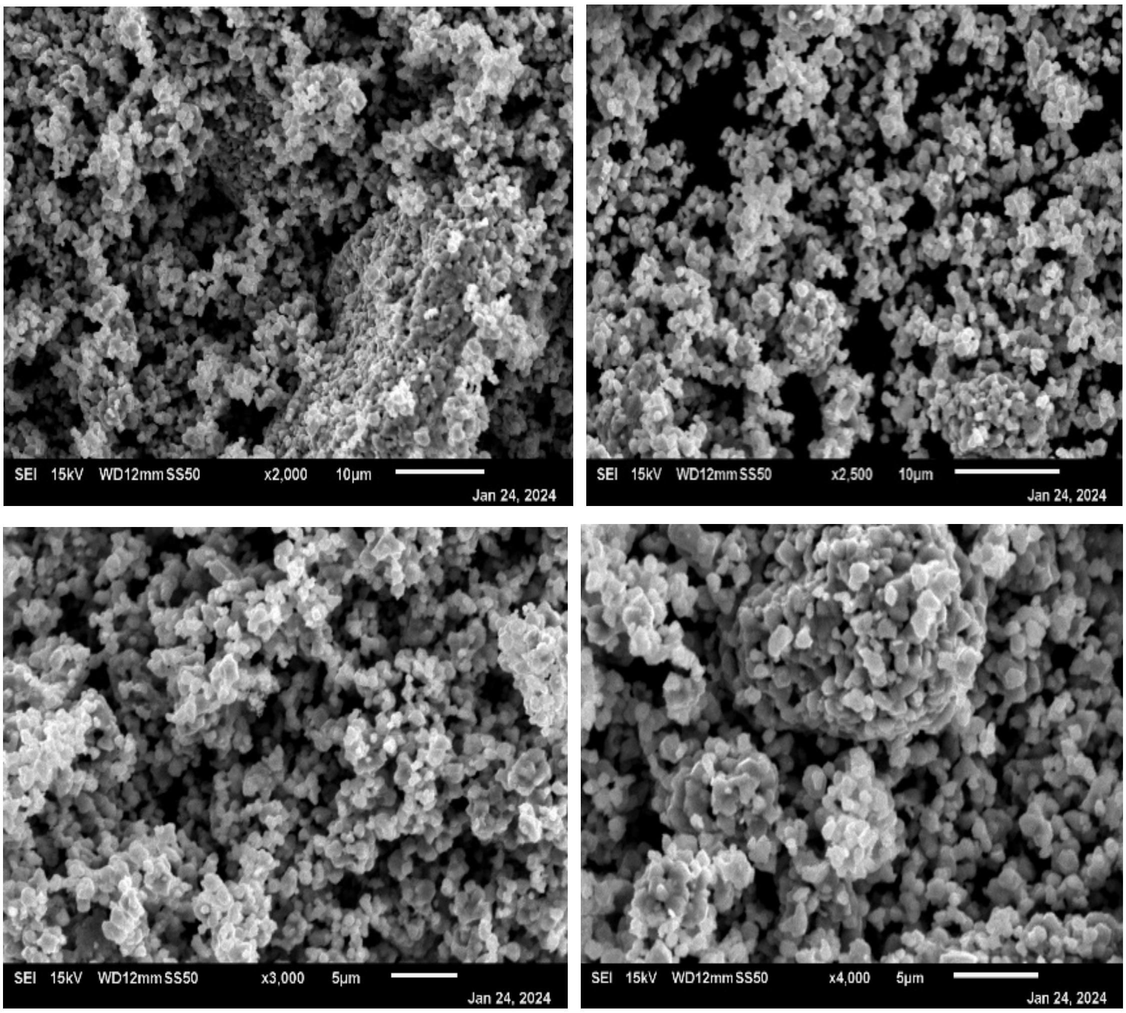

Figure 7. SEM micrographs of calcined $Sr_{0.5}Zn_{0.5}Mn_2O_4$ powder

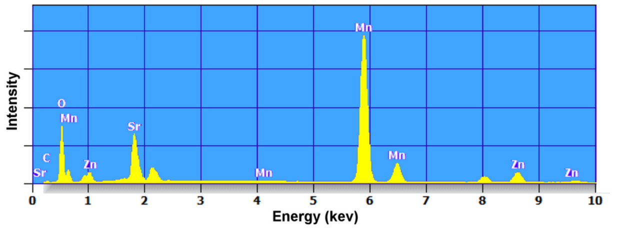

Content	O	Mn	Zn	Sr	C
[wt.%]	16.83	57.44	7.32	16.52	1.90
[at.%]	41.15	40.91	4.38	7.38	6.18

Figure 8. EDX spectra and elemental composition of $Sr_{0.5}Zn_{0.5}Mn_2O_4$ powder

Inset in Fig. 6 represents the curve $(\alpha h\nu)^2$ as a function of energy E where the point of intersection of the tangent with the energy axis directly gives the value of E_g. The plot of the optical density $(\alpha h\nu)^2$ as a function of energy ($h\nu$) shows that the synthesized $Sr_{0.5}Zn_{0.5}Mn_2O_4$ powder calcined at 900 °C has an energy band gap of 2.5 eV [74]. This energy value indicates that the prepared oxide demonstrates absorption activity in the visible region, allowing the excitation of this material with solar energy.

SEM analysis

SEM micrographs presented in Fig. 7 confirms that the $Sr_{0.5}Zn_{0.5}Mn_2O_4$ powder calcined at 900 °C consists of spherically shaped aggregates and has porous structure. All particles exhibit uniformity in size and shape. EDX measurements confirmed that the corresponding elements of the oxide $Sr_{0.5}Zn_{0.5}Mn_2O_4$ can be observed in the spectrum of the synthesized nanostructure (Fig. 8). The atomic percentages of Mn, Zn, Sr and O were 40.91%, 4.38%, 7.38% and 41.15%, respectively, suggesting the formation of a spinel-type structure in which strontium and zinc atoms substitute within the manganese spinel, resulting in the chemical formula $Sr_{0.5}Zn_{0.5}Mn_2O_4$. Elemental mapping and EDX analysis confirm the spatial distribution of these elements within the sample [71].

Point of zero charge

Point of zero charge (pH_{pZC}) test enables identifying the ideal pH needed to facilitate photocatalytic reactions. The photocatalytic process becomes more effective when it is performed at pH levels that promote the suitable surface charge in the process. For this we used the drift method to determine pH_{pZC} of the material [75]. The point of zero charge (pH_{pZC}) of an oxide material like $Sr_{0.5}Zn_{0.5}Mn_2O_4$ indicates the pH at which effective charge on the surface of this material is zero. Figure 9 shows that the pH_{pZC} of $Sr_{0.5}Zn_{0.5}Mn_2O_4$ is 6.8. Below this value, the charge of $Sr_{0.5}Zn_{0.5}Mn_2O_4$ surface is positive. This can improve the uptake of negatively charged entities (anions) from the solution such as pollutants or dye molecules containing anionic groups. This enhanced adsorption brings the pollutants into closer proximity to the photocatalyst, increasing the likelihood of photocatalytic degradation. Above pH = 6.8, the surface becomes negatively charged which favours the adsorption of positively charged species (cations). This could be advantageous or disadvantageous depending on the target pollutant. If the pollutant carries a positive charge, degradation will be enhanced. However, if the desired reaction involves negatively charged species, the photocatalytic efficiency might be reduced [76].

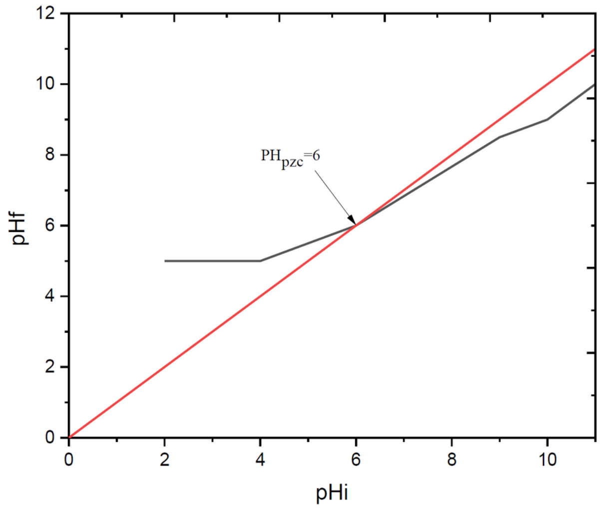

Figure 9. Determination of pH_{pZC} of $Sr_{0.5}Zn_{0.5}Mn_2O_4$

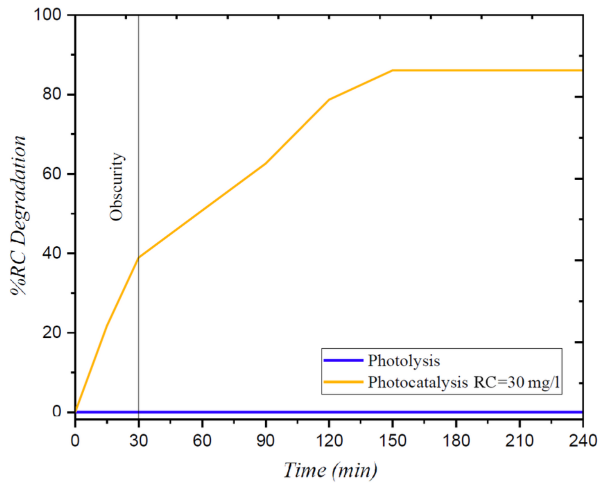

Figure 10. Degradation of RC at: [RC] = 30 mg/l, [catalyst] = 0.05 g/l, *V* = 100 ml, pH = 6

3.2. Photocatalytic activity

The photocatalytic activity of the $Sr_{0.5}Zn_{0.5}Mn_2O_4$ powder was evaluated by: i) irradiation of the RC solution under visible light in the absence of a catalyst, ii) adsorption of the RC solution in the presence of the catalyst in the dark for 30 min and iii) irradiation of the RC solution under visible light in the presence of the catalyst. The results are presented in Fig. 10 and indicate that direct photolysis did not result in a significant degradation under visible irradiation. In the presence of the catalyst without irradiation, a significant loss was observed due to the adsorption of RC onto the surface of the catalyst (Fig. 10). Irradiation under visible light in the presence of the catalyst caused degradation of RC ~90% within 150 min [77]. The photogeneration of radical species in the photocatalytic mechanism involves the absorption of light by the photocatalyst, which generates (e^-, h^+) pairs. This process can be described as follows [78]:

$$h\upsilon + (Sr_{0.5}Zn_{0.5}Mn_2O_4) \rightarrow h^+ + e^-$$
$$H_2O + h^+ \rightarrow H^+ + OH^\circ$$
$$O_2 + e^- \rightarrow O^{\circ -}_2$$
$$Dye + h^+ \rightarrow oxidation\ products$$
$$Dye + e^- \rightarrow reduction\ products$$

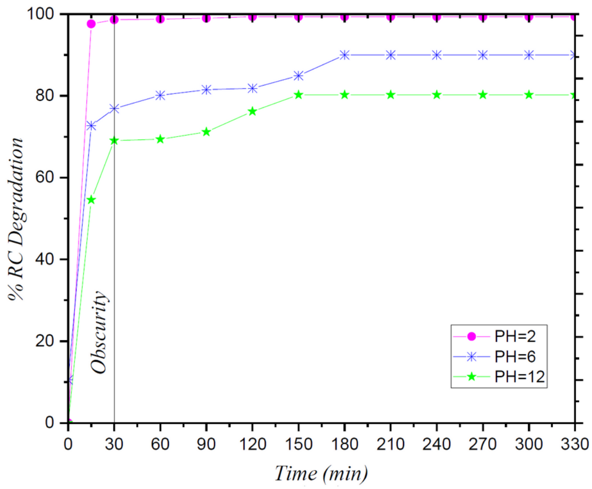

Figure 11. Effect of pH on the photocatalytic degradation of RC at: [catalyst] = 0.075 g/l, [RC] = 30 mg/l and *V* = 100 ml

Effect of pH on the degradation of RC dye

The effect of pH on the degradation of RC was investigated. The initial pH of the reaction solution was adjusted by the addition of concentrated sulphuric acid and sodium hydroxide solutions. The evolution of RC degradation as a function of time at different pH values is shown in Fig. 11. The degradation of RC is maximal in acidic environment and decreased with increasing pH. These results can be related to the surface charge of the catalyst (for the $Sr_{0.5}Zn_{0.5}Mn_2O_4$ powder pH_{PZC} = 6) and the ionization state of the dye. At pH = 2, positive charge is developed on the surface of the photocatalyst in conjunction with the negative charges of the red Congo dye, which results in an electrostatic attraction of the positive charge of $Sr_{0.5}Zn_{0.5}Mn_2O_4$ and the negative charge of the dye resulting in a strong adsorption of the molecule on the photocatalyst surface [79]. Thus, depending on the pH of the solution, the Coulomb attractive and repellent forces are fully involved in the process of dye degradation.

Effect of catalyst mass on the degradation of RC dye

The effect of the catalyst amount on the photocatalytic degradation of RC was investigated in a series of experiments to maintain the concentration of RC constant at 30 mg/l and to vary the amount of $Sr_{0.5}Zn_{0.5}Mn_2O_4$ from 0.025 to 0.1 g/l. The results shown in Fig. 12 confirm that the degradation of RC increases with increasing the mass of the catalyst up to an amount of 0.075 g/l, due to the number of active sites of the catalyst, and then a decrease in degradation at high catalyst amount (0.1 g/l) may be due to the reduction of light penetration with excess $Sr_{0.5}Zn_{0.5}Mn_2O_4$ amount [80].

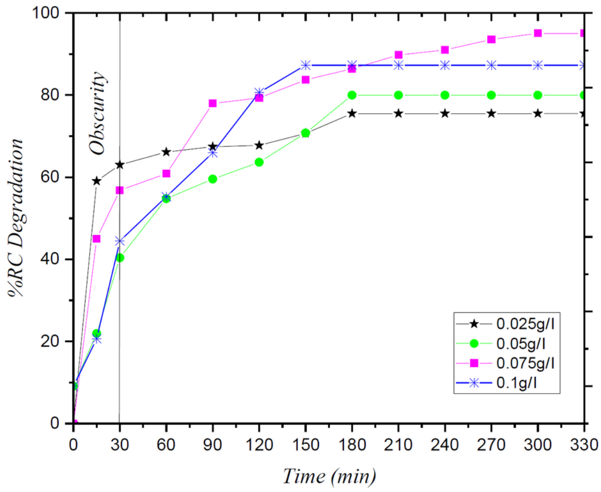

Figure 12. Effect of catalyst amount on photocatalytic degradation at: [RC] = 30 mg/l and *V* = 100 ml, pH = 6

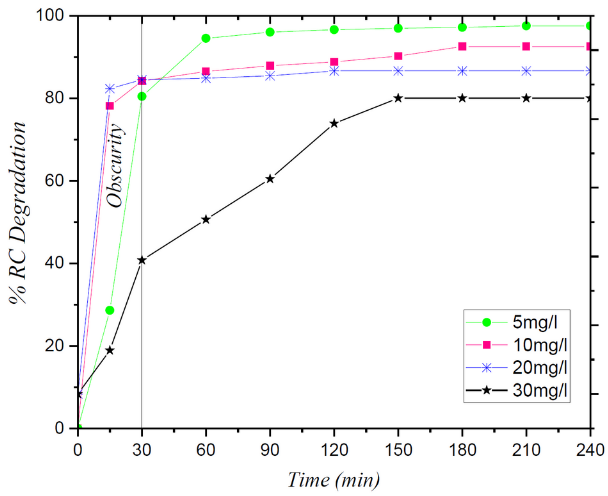

Figure 13. Effect of initial concentration of RC on photocatalytic degradation at: neutral pH [catalyst] = 0.1 g/l and *V* = 100 ml

Effect of initial concentration on the RC degradation

The effect of the initial concentration of Congo red (RC) was also investigated by varying the dye concentrations from 5 to 30 mg/l at a neutral pH, while maintaining a constant catalyst concentration of 0.1 g/l (Fig. 13). The results obtained indicate that the degradation of Congo red becomes increasingly significant as the concentration of RC decreases. This finding suggests that lower initial concentrations enhance the efficiency of the photocatalytic process, leading to the more effective degradation of the dye. The formation of hydroxyl (•OH) radicals on the catalyst surface and their reaction with dye molecules control the degradation rate. As dye concentrations increase, more dye molecules are adsorbed, leading to the reduction of the visible light penetration and decreased hydroxyl radical generation. This results in diminished degradation efficiency, as active sites become occupied and fewer free radicals are available to react with the dye. This observation is consistent with previous findings in the literature [81].

The presented results highlight the potential of $Sr_{0.5}Zn_{0.5}Mn_2O_4$ as a promising photocatalyst for environmental remediation, especially when it is compared with degradation efficiency of some other spinel oxides (Table 1).

Table 1. Maximum degradation efficiency of $Sr_{0.5}Zn_{0.5}Mn_2O_4$ versus other catalysts

Catalyst	Degradation [%]	Pollutant dye	Conditions	Ref.
$NiCo_2O_4$	60%	Cr(VI)	C=1mg/l, pH=6, RT, t=240 min	[82]
$ZnFe_2O_4$	90%	CR	C=10PPM, m=1g/l, RT, t=40 min	[59]
Mg-$ZnMn_2O_4$	72%	MB	C=30PPM, pH=10, m=1g/l, t=120 min	[58]
$CoFe_2O_4$	82.63%	Reactive Red 120	C=30PPM, pH=2, m=0.08g, t=90 min	[60]
$CuFe_2O_4$	55%	MB	C=10PPM, m=0.1g, t=120 min	[61]
$ZnMn_2O_4$	92.43%	MV	C=10PPM, m=0.03g, pH=6, t=90 min	[57]
$ZnFe_2O_4$	90.52	MV	C=20PPM, m=0.05g	[56]
$Sr_{0.5}Zn_{0.5}Mn_2O_4$	99.37	Red Congo	C=30PPM, m=0.075g, pH=2, t=150 min	this work

IV. Conclusions

In this study, we successfully synthesized a new $Sr_{0.5}Zn_{0.5}Mn_2O_4$ using the ultrasonic method, resulting in a material with a well-defined spinel structure. Characterization techniques confirmed the formation of uniformly sized porous nanoparticle aggregates, with significant vibrational peaks indicating Mn–O, Sr–O and Zn–O bonds. Optical properties revealed an energy band gap of 2.5 eV and a neutral surface charge at pH = 6.8, suggesting favourable conditions for photocatalytic activity. Degradation studies showed that $Sr_{0.5}Zn_{0.5}Mn_2O_4$ effectively degrades Congo red dye, achieving an efficiency of 99.37% within 150 min at an optimal pH of 2 and a catalyst dosage of 0.075 g/l, with improved degradation efficiency at higher initial dye concentrations. These results highlight the potential of $Sr_{0.5}Zn_{0.5}Mn_2O_4$ as a promising photocatalyst for environmental remediation, offering an effective solution for the degradation of organic pollutants in wastewater treatment. Further research could explore its applicability in various environmental contexts.

Acknowledgments: The authors would like to acknowledge the facilities provided by UAE University through research grant (12R227).

References

1. S.J. Peighambardoust, Z. Mahdavi, M. Gholizadeh, R. Foroutan, B. Ramavandi, "Pyrolytic carbon/Cloisite 30B/$ZnFe_2O_4$ as reclaimable magnetic nanocomposite for methylene blue decontamination", *Colloids Surfaces A: Physicochem. Eng. Aspects*, **704** (2025) 135543.
2. E. Safamariyam, K.P. Synumol, A.J. Panicker, M.S. Sha, S. Roshan, S.P. Dakua, V. Chandrasekar, A.V. Singh, K.K. Sadasivuni, "An insight into unveiling nano luminescence for industrial dye detection", *J. Fluorescence*, 2025, in press.
3. F.T.A. Appia, T.G.D. Kouassi, K.J. Kimou, C.S. Coulibaly, J.-C. Meledje, L. Ouattara, "Photolytic degradation of methylene blue: The effect of various factors on wastewater treatment efficiency", *Asian J. Chem. Sci.*, **15** [1] (2025). 41–52.
4. M.T. Agbadaola, D.A. Akinyemi, D.A. Olatunji, J.O. Babalola, "Fenton-like modification of Bauhinia tomentosa seedpod for improved sequestration of methylene blue from water", *Res. Square*, 2025, in press.
5. A. Saleem, A. Munawar, S. Kauser, "Removal of naphthol green B and indigo carmine from wastewater by wheat bran and urea-modified rice husk", *Environ. Monitoring Assess.*, **197** [3] (2025) 265.
6. A.B. Siddique, M.A. Shaheen, A. Abbas, Y. Zaman, M.Z. Ishaque, A. Shami, M. Aslam, K.M. Alsyaad, A. Ali, "Highly efficient greenly synthesized cadmium oxide nanoparticles for methyl orange degradation, antibacterial and antioxidant applications". *J. Mol. Struct.*, **1331** (2025) 141566.
7. L.T.T. Nguyen, H.T.T. Nguyen, L.T.H. Nguyen, N.V. Vu, H.T. Vu, H.T. Tran, H.Q. Nguyen, H.T.T. Dinh, T.V. Tran, "Facile synthesis of $ZnFe_2O_4$/bentonite composites and their utilization for photocatalytic

degradation of rhodamine B dye", *Int. J. Environ. Sci. Technol.*, **22** [11] (2025).

8. S.C. Yong, S.H. Shuit, W.Y. Tan, Q.H. Ng, S. Lim, H.S. Thiam, S.F. Tee, K.C. Chong, P.Y. Hoo, "Removal of methylene blue using trifunctional magnetic polyethersulfone microcapsule: Process parameters and optimization study:, *Int. J. Nanoelectron. Mater.*, **18** [1] (2025) 104–112.
9. H.C.T. Firmino, E.P. Nascimento, L.C.C. Arzuza, R.N. Araujo, B.V. Sousa, G.A, Neves, M.A. Morales, R.R. Menezes, "High-efficiency adsorption removal of Congo red dye from water using magnetic $NiFe_2O_4$ nanofibers: An efficient adsorbent", *Materials*, **18** [4] (2025) 754.
10. R. Etana, K. Angassa, T. Getu, "Dye removal from textile wastewater using scoria-based of vertical subsurface flow constructed wetland system", *Sci. Reports*, **15** [1] (2025) 949.
11. N. Roy, T. Nivedya, P. Paira, R. Chakrabarty, "Selenium-based nanomaterials: Green and conventional synthesis methods, applications, and advances in dye degradation", *RSC Advances*, **15** [4] (2025) 3008–3025.
12. A. Singh, A. Kumar, N. Kaur, N. Singh, „Chemically modified gelatin/chitosan as a chemosensor adsorbent for detection of toxic metals and removal of organic dyes", *Polym. Adv. Technol.*, **36** [1] (2025) e70088.
13. S. Panda, "Bioremoval of industrial dyes using different microorganisms", *J. Microbio. Infection*, **2** (2024) 10–14.
14. D. Karthigaimuthu, S. Ramasundaram, P. Nisha, B. Arjun Kumar, J. Sriram, G. Ramalingam, P. Vijaibharathy, T.H. Oh, T. Elangovan, "Synthesis of MoS_2/$Mg(OH)_2$/$BiVO_4$ hybrid photocatalyst by ultrasonic homogenization assisted hydrothermal methods and its application as sunlight active photocatalyst for water decontamination", *Chemosphere*, **308** (2022) 136406.
15. C.R. Michel, Rapid degradation of organic dyes by nanostructured Gd_2O_3 microspheres, *Appl. Nano*, **6** [1] (2025) 1.
16. S. Latif, A. Zahid, F. Batool, S. Kanwal, A. Ditta, "Adsorptive removal of Congo red dye from industrial effluent using cotton calyx iron oxide (CC-Fe_3O_4) composite", *Environ. Monitoring Assess.*, **197** [3] (2025) 249.
17. S. Sismanoglu, E. Buran, "Azo dye adsorption on ZrO_2 and natural organic material doped ZrO_2", *Sci. Reports*, **15** [1] (2025) 2842.
18. K. Dharmalingam, E. Thangavel, P.C. Tsai, P.V. Pham, K. Prakasham, G. Andaluri, K.B. Manjappa, Y.C. Lin, V.K. Ponnusamy, "Novel MoS_2-In_2O_3-WS_2 (2D/3D/2D) ternary heterostructure nanocomposite material: Efficient photocatalytic degradation of antimicrobial agents under visible-light", *Environ. Res.*, **261** (2024) 119759.
19. K. Dharmalingam, V. Gurudevan, G. Dhanasekaran, D. Sekar, R. Gopal, D. Alshamsi, E. Thangavel, S. Sambasivam, "Synthesis and characterization of lamellar-like $Cu_2(OH)_3NO_3$ nanosheets integrated with Mg(OH)2 nanoparticles heterojunction for photocatalytic activity", *J. Mater. Res.*, **39** [2] (2024) 231–247.
20. K. Dharmalingam, A.K. Bojarajan, R. Gopal, E. Thangavel, S.A. Burhan Al Omari, S. Sangaraju, "Direct Z-scheme heterojunction impregnated MoS_2–NiO–CuO nanohybrid for efficient photocatalyst and dye-sensitized solar cell", *Sci. Reports*, **14** [1] (2024) 1–20.
21. B. Arjun Kumar, T. Elangovan, D. Karthigaimuthu, D. Aravinth, G. Ramalingam, F. Ran, S. Sangaraju, "CdSe quantum dots bedecked on ZnO/TiO_2/CuO ternary nanocomposite for enhanced photocatalytic and photovoltaic applications", *Langmuir*, **39** [45] (2023) 15864–15877.
22. K. Dharamalingam, B. Arjun Kumar, G. Ramalingam, S. Sasi Florence, K. Raju, P. Senthil Kumar, S. Govindaraju, E. Thangavel, "The role of sodium dodecyl sulfate mediated hydrothermal synthesis of MoS_2 nanosheets for photocatalytic dye degradation and dye-sensitized solar cell application", *Chemosphere*, **294** (2022) 133725.
23. S. Kumar, A. Kaur, J. Gaur, P. Singh, H. Kaur, S. Kaushal, J. Dalal, M. Misra, "State-of-the-art in Co_3O_4 nanoparticle synthesis and applications: Toward a sustainable future", *ChemistrySelect*, **10** [6] (2025) e202405147.
24. C. Ben Makhlouf, M.L. Bouazizi, S. Hcini, H. Ben Bacha, L. HajTaieb, M. Gassoumi, "Detailed structural study, optical, and dielectric properties of $Co_{0.4}Ni_{0.3}Zn_{0.3}Fe_2O_4$ ferrite and its potential applications for optoelectronic and electronic devices", *J. Sol-Gel Sci. Technol.*, 2025, in press.
25. S. Sahu, V.S. Buddhiraju, V. Runkana, "A thermo-electrochemical model for capacity fading of spinel manganese oxide cathode-based Li-ion half cell", *J. Electrochem. Soc.*, **172** [2] (2025) 020517.
26. M.A. Hefnawy, R. Abdel-Gaber, S.M. Gomha, M.E.A. Zaki, S.S. Medany, "Synthesis of nickel-manganese spinel oxide supported on carbon-felt surface to enhance electrochemical capacitor performance", *Electrocatalysis*, **16** (2025) 500–512.
27. X. Liu, S. Yang, S. Li, T. Wang, X. Gao, Y. Chen, W. Zhang, "The doping of Al^{3+} at the tetrahedral site of spinel Mn_3O_4 for electrocatalytic water oxidation", *Chemistry - Eur. J.*, **31** [11] (2025) e202403720.
28. A. Sánchez-Caballero, J.M. Porras-Vázquez, L. dos Santos-Gómez, J. Zamudio-García, A. Infantes-Molina, J. Canales-Vázquez, E.R. Losilla, D. Marrero-López, "Structure and mixed proto-electronic conductivity in Pr and Nb-substituted $La_{5.4}MoO_{12-\delta}$ ceramics", *Materials*, **18** [3] (2025) 529.
29. K. Banerjee Ghosh, A. Balo, U. Utkarsh, M. Yasmine, U. Gosh, "Advancing spin controlled electrocatalysis using chiral gold nanoparticles functionalized bimetallic spinel oxide", *ChemCatChem*. 17 [7] (2025) e202401695
30. E.Y. Ardiansyah, M.S. Idris, R.A. Maulat Osman, F. Fahmi, "Effect of cation ordering on the structure, electrical and electronic properties of cubic spinel $LiNi_{0.5}Mn_{1.5}O_4$", *Int. J. Nanoelectron. Mater.*, **18** [1] (2025) 86–96.
31. C.-H. Yim, Z. Karkar, M.S.E. Houache, D. Kim, B. Jang, Y. Abu-Lebdeh, "Enabling 5V solid-state lithium metal batteries using catholyte for $LiNi_{0.5}Mn_{1.5}O_4$ spinel", *ECS Meeting Abstracts*, **MA2024-02** [7] (2024) 920.
32. S. Tazeen, Y. Nazia, K. Shazia, K. Arooma, N. Rubina, M. Hafiza, S. Muhammad, M. Misbah, "Solar

induced photocatalytic degradation of textile dyes using composite of indium oxide and silver vanadate”, *Canad. J. Chem*., **103** [4] (2025)
33. J. Asokan, P. Kumar, G. Arjunan, M.G. Shalini, “Photocatalytic performance of spinel ferrites and their carbon-based composites for environmental pollutant degradation”, *J. Cluster Sci.*, **36** [2] (2025). 42.
34. A., Hemmi, M., Belmedani, E., Mekatel, A.M. Djaballah, Z. Sadaoui, B. Brahimi, M. Trari, “Characterization of $MgAl_2O_4$ semiconductor prepared by co-precipitation route: application as photocatalyst for tetracycline degradation”, *J. Mater. Sci. Mater. Electron.*, **36** [3] (2025) 217.
35. N. Mohammad Hosseini, S. Sheshmani, A.S. Shahvelayati, “Manganese ferrite-graphite oxide-chitosan nanocomposite for efficient dye removal from aqueous and textile wastewater under UV and sunlight irradiation”, *Sci. Reports*, **15** [1] (2025) 866.
36. R. Prasetyowati, R.I. Saputri, E.F.M. Harahap, P.E. Swastika, F. Fauzi, W.S.B. Dwandaru, A. Ariswan, M. Riswan, E. Widianto, “Fe_3O_4/graphene oxide derived from natural iron sand for enhanced photocatalytic degradation of rhodamine-B textile dye waste”, *Emergent Mater*., 2025, in press.
37. J. Ahmad, A. Ikhlaq, M. Raashid, U. Ikhlaq, U.Y. Qazi, H.T. Masood, T. Hussain, M. Kazmi, N. Ramzan, A. Naeem, A. Aly Hassan, F. Qi, R. Javaid, “Novel $AlCo_2O_4$/MWCNTs nanocomposites for efficient degradation of reactive yellow 160 dye: Characterization, photocatalytic efficiency, and reusability”, *Catalysts*, **15** [2] (2025) 154.
38. S. Haffas, N. Belhamra, Z. Bencharef, N. Redjouh, B. Gasmi, S. Rahmane, “Impact of copper-doped cobalt oxide thin films on the photocatalytic degradation of methylene blue dye under sunlight irradiation”, *React. Kinet. Mechanisms Catal.*, **138** (2025) 1747–1764.
39. R. Katoh, “Photoionization-induced charge separation for efficient solar energy conversion”, *J. Chem. Phys.*, **162** [5] (2025) 050901.
40. E. Todarello, *Axion-Like Particle Conversion in the Solar Magnetic Field*, arXiv:2501.15960, Cornel University, 2025.
41. K.K. Saravanan, D. Venkatesan, R. Regan, G. Hariharan, “Optimizing dye-sensitized solar cells with a TiO_2/CoS hybrid photoanode for enhanced solar energy conversion”, *Ionics*, **31** (2025) 3575–3589.
42. B. Liu, O.J. Sandberg, J. Qin, Y. Liu, S. Wilken, N. Wu, X. Yu, J. Fang, Z. Li, R. Huang, W. Zha, Q. Luo, H. Tan, R. Österbacka, C.Q. Ma, “Inverted organic solar cells with an in situ-derived SiO_xN_y passivation layer and power conversion efficiency exceeding 18%”, *Nat. Photonics*, **19** (2025) 195–203.
43. P. Sharma, R.K. Mishra, A. Panda, K. Palodhi, “The effect of indium tin oxide (ITO) nanowire on perovskite thin film solar cells”, *J. Electron. Mater.*, **54** (2025) 2797–2809.
44. R. Zhang, C. Qin, H. Bala, Y. Wang, J. Cao, “Recent progress in spinel ferrite (MFe_2O_4) chemiresistive based gas sensors”, *Nanomaterials*, **13** [15] (2023) 2188.
45. N. Hiratsuka, H. Kobayashi, H. Uchida, T. Katsube, “Gas sensing characteristics of zinc-tin complex oxide thin films with spinel-type structure”, *J. Ceram. Soc. Jpn.*, **104** [11] (1996) 1048–1051.
46. C.J. Belle, A. Bonamin, U. Simon, J. Santoyo-Salazar, M. Pauly, S. Bégin-Colin, G. Pourroy, “Size dependent gas sensing properties of spinel iron oxide nanoparticles”, *Sensor. Actuat. B Chem.*, **160** [1] (2011) 942–950.
47. S. Helali, Z. Landolsi, I.B. Assaker, “Advanced metal oxide nanostructures for environmental remediation: Synthesis and characterization of PbO, MgO, TiO_2 and Fe_2O_3”, *Chem. Mater. Sci. Develop. Innov.*, **8** (2024) 68–91.
48. Komal, S. Singh, S. Bansal, S. Singhal, “Spinel nanoferrites: A versatile platform for environmental remediation”, pp. 315–347 in *Topics in Mining, Metallurgy and Materials Engineering*, Springer Nature, 2021.
49. D.B. Olawade, O.Z. Wada, B.I. Egbewole, O. Fapohunda, A.O. Ige, S.O. Usman, O. Ajisafe, (2024). Metal and metal oxide nanomaterials for heavy metal remediation: novel approaches for selective, regenerative, and scalable water treatment. *Front. Nanotechnol.*, 6 (2024) 1466721.
50. P. Bhatia, P. Bansal, R. Chandra, “Advancements in metal Oxide/polymer nanocomposite utilized as photocatalysts for wastewater remediation”, pp. 215–236 in *Hybrid Composite Materials*,. Springer Nature, 2024.
51. A. Venkateshaiah, M. Černík, V.V.T. Padil, “Metal oxide nanoparticles for environmental remediation”, pp. 183–213 in *Nanotechnology for Environmental Remediation*, Wiley, 2022.
52. J., Prakash, R. Jasrotia, Suman, P. Kotwal, Himanshi, A. Verma, A. Kandwal, P. Kumar, S.K. Godara, “Spinel nanoferrites: Adsorption and photocatalysis of emerging pollutants”, pp. 31–55 in *Nanomaterials: An Approach Towards Environmental Remediation*, Bentham Science, 2024.
53. J., Ding, L. Zhang, Z. Wei, Z. Wang, Q. Liu, G. Hu, J. Luo, X. Liu, “Coupling nitrate-to-ammonia conversion and sulfion oxidation reaction over hierarchical porous spinel MFe_2O_4 (M = Ni, Co, Fe, Mn) in wastewater”, *Small*., **21** [7] (2025) 2411317.
54. A. Goyal, M. Dhiman, “Emerging role of ferrite nanostructures for the remediation of environmental pollution”, pp. 99–120 in *Nanomaterials: An Approach Towards Environmental Remediation*, Bentham Science, 2024.
55. G.S. Amgith, N. Pathak, R.K. Pilania, M. Ranjan, C.L. Dube, “Microwave-assisted synthesis of graphene oxide–cobalt ferrite magnetic nanocomposite for water remediation”, *Bull. Mater. Sci.*, **47** [4] (2024) 277.
56. A.M. Fallatah, S.D. Alahmari, H.M.T. Farid, “Facile synthesis of the MOF derived $ZnMn_2O_4$ nanorods for dyes degradation in water”, *J. Mater. Sci. Mater. Electron.*, **34** [22] (2023) 1630.
57. A. Sobhani, S. Alinavaz, “$ZnMn_2O_4$ nanostructures: Synthesis via two different chemical methods, characterization, and photocatalytic applications for the degradation of new dyes”, *Heliyon*, **9** [11] (2023) e21979.
58. R. Gherbi, M. Benamira, Y. Bessekhouad, “Enhanced photoelectrochemical and photocatalytic properties of Mg-doped $ZnMn_2O_4$”, *J. Alloys Compd.*, **851** (2021) 156797.
59. Z.A. Mohammed Nazeer, M. Praveen, R. Harikrishna, M. Kumar, S. Nagarajaiah, B.M.

Nagabhushana, Photocatalytic Degradation of the Azo Dye “Congo-Red” by $ZnFe_2O_4$/ ZnO Nanocomposite. *J. Mines Metals Fuels*, **71** [12A] (2024) 192–199.

60. M. Parastar Gharehlar, S. Sheshmani, F.R. Nikmaram, Z. Doroudi, “Synergistic potential in spinel ferrite MFe_2O_4 (M = Co, Ni) nanoparticles-mediated graphene oxide: Structural aspects, photocatalytic, and kinetic studies”, *Sci. Reports*, **14** [1] (2024) 4625.
61. D. Zala, A.K. Mishra, I. Mukhopadhyay, A. Ray, “Structure-led manifestation of photocatalytic activity in magnetically recoverable spinel $CuFe_2O_4$ nanoparticles and its application in degradation of industrial effluent dyes under solar light”, *Nanotechnology*, **35** [29] (2024) 295701.
62. M. Yaqoubi, M. Salavati-Niasari, M. Ghanbari, “S-scheme $CuMn_2O_4$/g-C_3N_4 heterojunction: fabrication, characterization, and investigation of photodegradation potential of organic pollutants”, *Appl. Water Sci.*, **15** [1] (2025) 13.
63. P. Shinde, Y. Hase, V. Doiphode, B.R. Bade, D. Kale, S. Rahane, J. Thombare, D. Borkar, S.R. Rondiya, M. Prasad, S.P. Patole, S.R. Jadkar, “Morphology-dependent ZnO/MoS_2 heterostructures for enhanced photoelectrochemical water splitting”, *ACS Appl. Energy Mater.*, **8** [2] (2025) 935 – 948.
64. L. Liu, W. Tang, L. Zuo, H. Fan, B. Li, L. Wang, “Fabrication of $ZnMn_2O_4$@$ZnIn_2S_4$ ball-in-ball hollow microspheres as efficient photocatalysts for hydrogen evolution”, *Inorg. Chem. Frontiers*, **11** [19] (2024) 6455–6466.
65. J.P. Morán-Lázaro, E.S. Guillen-López, F. López-Urias, E. Muñoz-Sandoval, O. Blanco-Alonso, H. Guillén-Bonilla, A. Guillén-Bonilla, V.M. Rodríguez-Betancourtt, M. Sanchez-Tizapa, M.D.L.L. Olvera-Amador, “Synthesis of $ZnMn_2O_4$ nanoparticles by a microwave-assisted colloidal method and their evaluation as a gas sensor of propane and carbon monoxide”, *Sensors* **18** [3] (2018) 701.
66. S. Deepika, N. Sivakumar, T. Jothilakshmi, R. Viji, R. Ramesh, “MOF-derived dessert rose like $ZnMn_2O_4$ electrode material for high-performance supercapacitors”, *Ionics*, **31** (2024) 945–952.
67. Z. Azmoodeh, S. Nasirian, H. Milani Moghaddam, “Improving H_2 gas sensing with $ZnMn_2O_4$/polypyrrole nanocomposite. *Int. J. Hydrogen Energy*, **85** (2024) 854–864.
68. S. Mahalakshmi, N. Hema, P.P. Vijaya, “In vitro biocompatibility and antimicrobial activities of zinc oxide nanoparticles (ZnO NPs) prepared by chemical and green synthetic route - A comparative study”, *BioNanoSci.*, **10** (2020) 112–121.
69. Y. Ghaffari, N. Kumar Gupta, J. Bae, K.S. Kim, “One-step fabrication of Fe_2O_3/Mn_2O_3 nanocomposite for rapid photodegradation of organic dyes at neutral pH”, *J. Mol. Liquids*, **315** (2020) 113691.
70. S.V. Mousavi, G.N. Bidhendi, N. Mehrdadi, “Synthesis of graphene oxide decorated with strontium oxide (SrO/GO) as an efficient nanocomposite for removal of hazardous ammonia from wastewater”, *Separat. Sci. Technol.*, **55** (2020) 1462–1472.
71. S. Soualmi, M. Henni, L. Djahnit, H. Hamdani, “Sol-gel synthesized ZnO-$SrMn_2O_4$ nanocomposite and its antibacterial properties”, *Eur. J. Chem.*, **29** [4-116] (2024) 71–81.
72. M. Molenda, R. Dziembaj, E. Podstawka, L.M. Proniewicz, “Changes in local structure of lithium manganese spinels (Li:Mn=1:2) characterised by XRD, DSC, TGA, IR, and Raman spectroscopy”, *J. Phys. Chem. Solids*, **66** (2005) 1761–1768.
73. A. Kadari, K. Mahi, R. Mostefa, M. Badaoui, A. Mameche, D. Kadri, “Optical and structural properties of Mn doped $CaSO_4$ powders synthesized by sol-gel process”, *J. Alloys Compd.*, **688** (2016) 32–36
74. F. Di Quarto, A. Zaffora, F. Di Franco, M. Santamaria, “Modeling of optical band-gap values of mixed oxides having spinel structure AB_2O_4 (A = Mg, Zn and B = Al, Ga) by a semiempirical approach”, *ACS Org. Inorg. Au*, **4** (2024) 120–134.
75. H. Sehil, M. Badaoui, A. Chougui, “Preparation and characterization of a novel chemically crosslinked chitosane-*g*-polyacrylamide hydrogel as a promising adsorbent for the removal of methylene blue from aqueous solutions”, *Polym. Sci. Ser. B*, **63** (2021) 853–865.
76. E.A. Al-Maliky, H.A. Gzar, M.G. Al-Azawy, “Determination of point of zero charge (PZC) of concrete particles adsorbents”, *IOP Conf. Ser.: Mater. Sci. Eng.*, **1184** (2021) 012004.
77. S. Ristig, N. Cibura, J. Strunk, “Manganese oxides in heterogeneous (photo)catalysis: Possibilities and challenges”, *Green*, **5** [1-6] (2015) 23–41.
78. R. Hazrati Saadabadi, F. Shariatmadar Tehrani, Z. Sabouri, M. Darraudi, “Photocatalytic activity and anticancer properties of green synthesized ZnO-MgO-Mn_2O_3 nanocomposite via *Ocimum basilicum* L. seed extract”, *Sci Rep.*, **14** (2024) 29812.
79. K.-H. Wang, Y.-H. Hsieh, C.-H. Wu, C.-Y. Chang, “The pH and anion effects on the heterogeneous photocatalytic degradation of o-methylbenzoic acid in TiO_2 aqueous suspension”, *Chemosphere*, **40** (2000) 389–394.
80. N. Elaziouti, Laouedj B. Ahmed, “ZnO-assisted photocatalytic degradation of Congo red and benzopurpurine 4B in aqueous solution”, *J. Chem. Eng. Process. Technol.*, **2** (2011) 106.
81. K.M. Reza, A. Kurny, F. Gulshan, “Parameters affecting the photocatalytic degradation of dyes using TiO_2: A review”, *Appl. Water Sci.*, **7** (2017) 1569–1578.
82. N. Cárdenas, H. Alarcon, T. Schnabel, S. Mehling, “Synthesis and characterization of nickel cobaltite–supported film for hexavalent chromium photocatalytic reduction”, *Water Sci. Technol.*, **90** [7] (2024) 2131–2145.